CrossMark

Migratory Outbursting Quasi-Hilda Object 282P/(323137) 2003 BM80[***]

Colin Orion Chandler [ID], William J. Oldroyd [ID], and Chadwick A. Trujillo [ID]
Department of Astronomy and Planetary Science, Northern Arizona University, PO Box 6010, Flagstaff, AZ 86011, USA; orion@nau.edu

Abstract

We report that object 282P/(323137) 2003 BM_{80} is undergoing a sustained activity outburst, lasting over 15 months thus far. These findings stem in part from our NASA Partner Citizen Science project Active Asteroids (http://activeasteroids.net), which we introduce here. We acquired new observations of 282P via our observing campaign (Vatican Advanced Technology Telescope (VATT), Lowell Discovery Telescope (LDT), and the Gemini South telescope), confirming 282P was active on UT 2022 June 7, some 15 months after 2021 March images showed activity in the 2021–2022 epoch. We classify 282P as a member of the quasi-Hilda objects (QHOs), a group of dynamically unstable objects found in an orbital region similar to, but distinct in their dynamical characteristics to, the Hilda asteroids (objects in 3:2 resonance with Jupiter). Our dynamical simulations show 282P has undergone at least five close encounters with Jupiter and one with Saturn over the last 180 yr. 282P was most likely a Centaur or Jupiter-family comet (JFC) 250 yr ago. In 350 yr, following some 15 strong Jovian interactions, 282P will most likely migrate to become a JFC or, less likely, an outer main-belt asteroid orbit. These migrations highlight a dynamical pathway connecting Centaurs and JFCs with quasi-Hildas and, potentially, active asteroids. Synthesizing these results with our thermodynamical modeling and new activity observations, we find volatile sublimation is the primary activity mechanism. Observations of a quiescent 282P, which we anticipate will be possible in 2023, will help confirm our hypothesis by measuring a rotation period and ascertaining the spectral type.

Unified Astronomy Thesaurus concepts: Hilda group (741); Comet dynamics (2213); Comet tails (274); Centaur group (215); Asteroid dynamics (2210)

1. Introduction

Volatiles are vital to life as we know it and are critically important to future space exploration, yet basic knowledge about where volatiles (e.g., H_2O, CO, CH_4) are located within our own solar system is still incomplete. Moreover, the origin of solar system volatiles, including terrestrial water, remains inconclusive. Investigating sublimation-driven active solar system bodies can help answer these questions (Hsieh & Jewitt 2006; Jewitt & Hsieh 2022).

We define volatile reservoirs as a dynamical class of minor planets that harbor volatile species, such as water ice. Comets have long been known to contain volatiles, but other important reservoirs are coming to light, such as active asteroids—objects on orbits normally associated with asteroids, such as those found in the main belt, that surprisingly display cometary features such as tails and/or comae (Jewitt et al. 2015). Fewer than 30 active asteroids have been discovered (Chandler et al. 2018)

since the first, (4015) Wilson–Harrington, was discovered in 1949 (Cunningham 1950) and, as a result, they remain poorly understood.

One scientifically important subset of active asteroids consists of members that display recurrent activity attributed to sublimation: the main-belt comets (MBCs; Hsieh et al. 2015). An important diagnostic of indicator sublimating volatiles, like water ice, is recurrent activity near perihelion (Hsieh et al. 2012; Snodgrass et al. 2017), a feature common to the MBCs (Hsieh et al. 2015; Agarwal et al. 2017; Hsieh et al. 2018). Fewer than 10 recurrently active MBCs have been discovered (though others exhibit activity attributed to sublimation), and as a result we know very little about this population.

Another potential volatile reservoir, active Centaurs, came to light after comet 29P/Schwassmann–Wachmann 1 (Schwassmann & Wachmann 1927) was identified as a Centaur following the 1977 discovery of (2060) Chiron (Kowal & Gehrels 1977). Centaurs, found between the orbits of Jupiter and Neptune, are cold objects thought to primarily originate in the Kuiper Belt prior to migrating to their current orbits (see review, Jewitt 2009). The dynamical properties of these objects are discussed in Section 5. Fewer than 20 active Centaurs have been discovered to date; thus they, like the active asteroids, are both rare and poorly understood.

In order to enable the study of active objects in populations not typically associated with activity (e.g., near-Earth objects (NEOs), main-belt asteroids), we created a Citizen Science project designed to identify roughly 100 active objects via volunteer identification of activity in images of known minor planets. The Citizen Science paradigm involves concurrently crowdsourcing tasks yet too complex for computers to perform, while also carrying out an outreach program that engages the
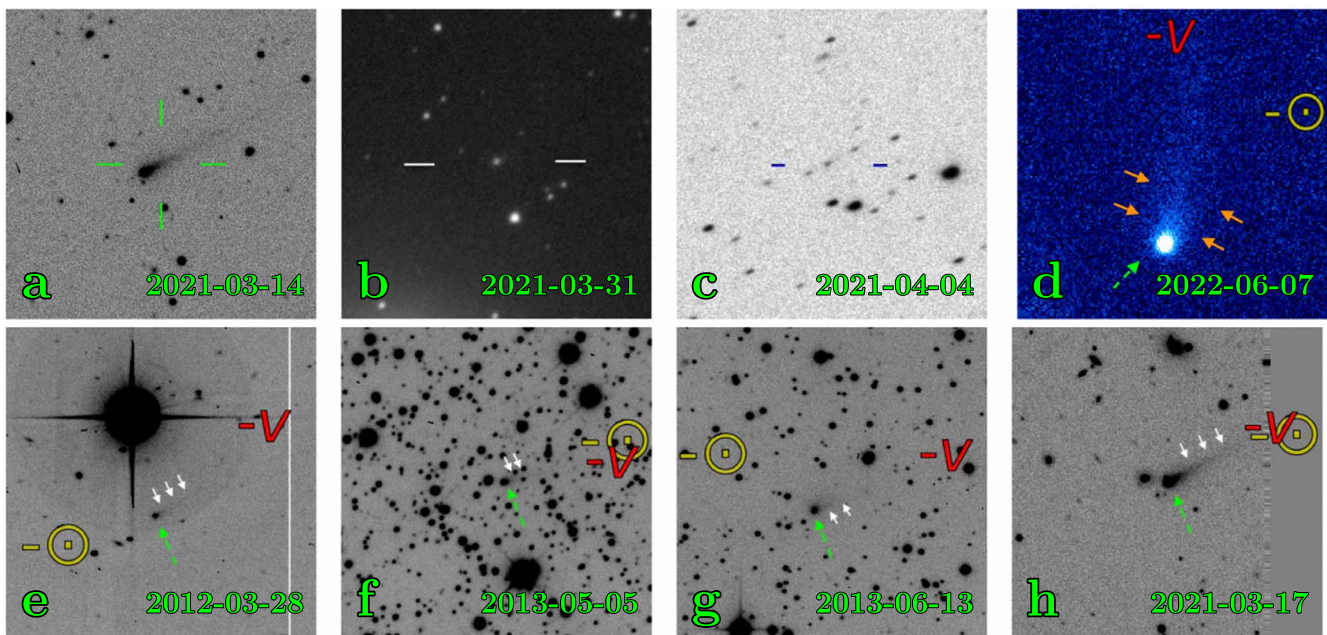

Figure 1. Top row: four images, spanning 15 months, showing 282P/(323137) 2003 BM$_{80}$ activity during the recent 2021–2022 activity epoch. (a) Epoch II thumbnail image of 282P was classified as "active" by 14 of 15 volunteers of our Citizen Science project *Active Asteroids*, a NASA Partner program. This 90 s *i*-band image was taken with the Dark Energy Camera on UT 2021 March 14, Prop. ID 2019A-0305 (PI Drlica-Wagner). (b) Epoch II, 12×300 s coadded exposures imaged by Michael Jäger with a QHY600 camera on a 14″ Newtonian telescope in Weißenkirchen, Austria. Image reproduced with permission of Michael Jäger. (c) Epoch II 5×300 s coadded images captured by Roland Fichtl using a CDS cooled Canon 5D Mark III camera on a 16″ Newtonian telescope in Engelhardsberg, Germany. Image reproduced with permission of Roland Fichtl. (d) For this most recent Epoch II image we coadded six 120 s *g′* band images of 282P (green dashed arrow) that we acquired on UT 2022 June 7 with the GMOS imager on the 8.1 m Gemini South telescope (Prop. ID GS-2022A-DD-103, PI Chandler); a tail is clearly visible (orange arrows). Bottom row: archival images of 282P that show clear evidence of activity. For each $126″ \times 126″$ thumbnail image, north is up and east is left. With the center of each image as the origin, the antisolar (yellow -$\odot$) and antimotion (red -*v*) directions (often correlated with tail appearance) are indicated. 282P is indicated by the green dashed arrow, and visible activity is marked by the white arrows. (e) Epoch I image from UT 2012 March 28 MegaPrime 120 s *r* band, Prop. ID 12AH16 (PI Wainscoat). (f) Epoch I image from UT 2013 May 5 DECam 150 s *r* band, Prop. ID 2013A-0327 (PI Rest). (g) Epoch I image from UT 2013 June 13 MegaPrime 120 s *r* band, Prop. ID 13AH09 (PI Wainscoat). (h) Epoch II image from UT 2021 March 17 DECam 90 s *i* band, Prop. ID 2019A-0305 (PI Drlica-Wagner).

public in a scientific endeavor. Launched in Fall 2021, our NSF funded, NASA partner program *Active Asteroids*[1] immediately began yielding results.

282P/(323137) 2003 BM$_{80}$, hereafter 282P, was originally discovered as 2003 BM$_{80}$ on UT 2003 Jan 31 by Brian Skiff of the Lowell Observatory Near-Earth-Object Search (LONEOS) survey, and independently as 2003 FV$_{112}$ by the Lincoln Near-Earth Asteroid Research (LINEAR) on UT 2003 Apr 18. 282P was identified to be active during its 2012–2013 epoch (centered on its perihelion passage) in 2013 (Bolin et al. 2013). Here, we introduce an additional activity epoch, spanning 2021–2022.

In this work we (1) present our National Aeronautics and Space Administration (NASA) Partner Citizen Science project *Active Asteroids*; (2) describe how volunteers identified activity that led to our investigation into 282P; (3) present (a) archival images and (b) new observations of 282P that show it has undergone periods of activity during at least two epochs (2012–2013 and 2021–2022) spanning consecutive perihelion passages; (4) classify 282P as a QHO; (5) explore the migratory nature of this object through dynamical modeling, including identification of a dynamical pathway between QHOs and active asteroids; and (6) determine volatile sublimation as the most probable activity mechanism.

2. Citizen Science

We prepared thumbnail images (e.g., Figure 1(a)) for examination by volunteers of our NASA Partner Citizen Science project *Active Asteroids*, hosted on the Zooniverse[2] online Citizen Science platform. First we extract thumbnail images from publicly available precalibrated Dark Energy Camera (DECam) archival images using a pipeline, Hunting for Activity in Repositories with Vetting-Enhanced Search Techniques (HARVEST), first described in Chandler et al. (2018) and expanded upon in Chandler et al. (2019, 2020, 2021). Each $126″ \times 126″$ thumbnail image shows one known minor planet at the center of the frame. We optimize the Citizen Science process by automatically excluding thumbnail images based on specific criteria, for example, when (a) the image depth is insufficient for detecting activity, (b) no source was detected in the thumbnail center, and (c) too many sources were in the thumbnail to allow for reliable target identification; see Chandler (2022) for an in-depth description.

Our workflow is simple: we show volunteers an image of a known minor planet and ask whether or not they see evidence of activity (like a tail or coma) coming from the object at the center of the image, as marked by a reticle (Figure 1(a)). Each thumbnail is examined by at least 15 volunteers to minimize volunteer bias. To help train volunteers and validate that the project is working as intended, we created a training set of thumbnail images that we positively identified as showing

activity, consisting of comets and other active objects, such as active asteroids. Training images are injected at random, though the interval of injection decays over time so that experienced volunteers only see a training image 5% of the time.

We take the ratio of "positive for activity" classifications to the total number of classifications the object received, as a score to estimate the likelihood of the object being active. Members of the science team visually examine all images with a likelihood score of ⩾80% and flag candidates that warrant archival image investigation and telescope follow-up (Section 3). We also learn of activity candidates through Zooniverse forums where users interact with each other, moderators, and our science team. Volunteers can share images they find interesting, which has, in turn, led us directly to discoveries.

As of this writing, over 6600 volunteers have participated in *Active Asteroids*. They have conducted over 2.8×10^6 classifications, completing assessment of over 171,000 thumbnail images. One image of 282P from UT 2021 March 14 (Figure 1(a)) received a score of 93% after 14 of 15 volunteers classified the thumbnail as showing activity. A second image from UT 2021 March 17 (Figure 1(h)) was classified as active by 15 of 15 volunteers, providing additional strong evidence of activity from 2021 March.

3. Observations

3.1. Archival Data

For each candidate active object stemming from *Active Asteroids* we conduct an archival data investigation, following the procedure described in Chandler et al. (2021). For this task, we query public astronomical image archives and identify images that may show 282P in the field of view (FOV). We download the data, extract thumbnail images centered on 282P, and visually examine all images to search for evidence of activity.

After visually inspecting >400 thumbnail images we found 57 images (listed in Section A) in which we could confidently identify 282P in the frame. The remaining images either did not probe faintly enough, did not actually capture 282P (e.g., 282P was not on a detector), or suffered from image artifacts that made the image unsuitable for activity detection. The 57 images span 22 observing dates; nine dates had at least one image we ascertained showed probable activity, five from the 2012 to 2013 epoch and four dates from the 2021 to 2022 apparition. Section 3 provides a complete list of observations used in this work.

Figure 2 shows three plots with shared *x*-axes (years). Apparent magnitude and observability (the number of hours an object is above the horizon and the Sun is below the horizon) together provide insight into potential observational biases. For example, observations for detecting activity are ideal when 282P is brightest, near perihelion, and observable for many hours in an observing night. When contrasting hemispheres, this plot makes it clear that some periods (e.g., 2016–2020) are more favorable for observations in the northern hemisphere, whereas other observation windows (e.g., 2013–2015, 2022) are better suited to southern hemisphere facilities.

3.2. Follow-up Telescope Observations

Magellan—During twilight on UT 2022 March 7 we observed 282P with the Inamori-Magellan Areal Camera and Spectrograph (IMACS) instrument (Dressler et al. 2011) on the Magellan 6.5 m Baade telescope located atop Las Campanas Observatory (Chile). We successfully identified 282P in the images; however, 282P was in front of a dense part of the Milky Way, preventing us from unambiguously identifying activity. We used these observations to inform our Gemini signal-to-noise ratio (S/N) calculations.

VATT—On UT 2022 April 6 we observed 282P with the 1.8 m Vatican Advanced Technology Telescope (VATT) at the Mount Graham International Observatory (MGIO) in Arizona (Proposal ID S165, Principal Investigator (PI) Chandler). 282P was in an especially dense part of the galaxy so we conducted test observations to assess the viability of activity detection under these conditions. We concluded object detection would be challenging and activity detection essentially impossible in such a dense field.

LDT—On UT 2022 May 21 we observed 282P with the Lowell Discovery Telescope (LDT) in Arizona (PI: Chandler). Finding charts indicated 282P was in a less dense field compared to our VATT observations; however we were hardly able to resolve 282P or identify any activity because the field was still too crowded.

Gemini South—On UT 2022 June 7 we observed 282P with the Gemini Multi-Object Spectrograph (GMOS) South instrument (Hook et al. 2004; Gimeno et al. 2016) on the 8.1 m Gemini South telescope located atop Cerro Pachón in Chile (Proposal ID GS-2022A-DD-103, PI Chandler). We timed this observation to take place during a ∼10 day window when 282P was passing in front of a less dense region of the Milky Way. We acquired 18 images, 6 each in *g'*, *r'*, and *i'*. Activity was clearly visible in the reduced data in all filters, with activity appearing strongest in *g'* (Figure 1(d)). Our observations confirmed 282P was still active, 15 months after the 2021 archival data, evidence supporting sublimation as the most likely cause for activity (Section 7).

4. Dynamical Modeling

We analyzed 282P orbital characteristics in order to (1) determine its dynamical class (Section 5), and (2) inform our activity mechanism assessment (Section 7). We simulated a cloud of 500 282P orbital clones, randomly drawn from Gaussian distributions centered on the current fitted parameters of 282P, with widths corresponding to uncertainties of those fits (Appendix C lists the parameters and associated uncertainties), as reported by JPL Horizons (Giorgini et al. 1996).

We modeled the gravitational influence of the Sun and the planets (except Mercury) on each orbital clone using the `Integrator with Adaptive Step-size control, 15th order (IAS15)` *N*-body integrator (Rein & Spiegel 2015), typically accurate to machine precision, with the `REBOUND Python` package[3] (Rein & Liu 2012; Rein et al. 2019). We ran simulations 1000 yr forward and backward through time. Longer integrations were unnecessary because dynamical chaos ensues prior to ∼200 yr ago and after ∼350 yr into the future; thus no meaningful orbital elements can be derived outside of this window.
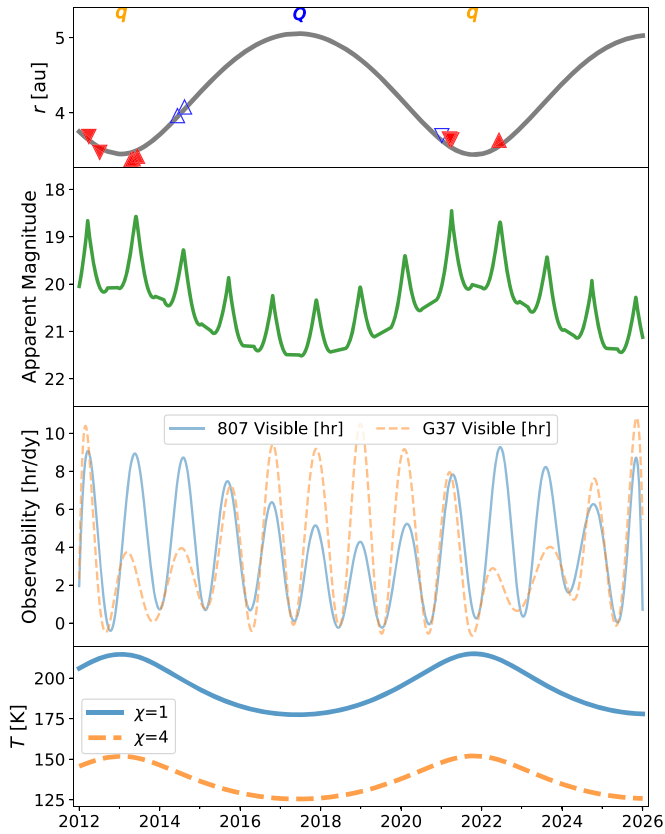
---

[3] https://github.com/hannorein/rebound

Figure 2. 282P heliocentric distance, observability, apparent brightness, observability, and temperature, from 2012 through 2025. Heliocentric Distance: Activity detections (triangles) are marked as positive (filled red) and negative (unfilled blue) detections and as either inbound (▼) or outbound (▲). Observations are cataloged in Appendix A. Also indicated are perihelion (orange q) and aphelion (blue Q) passages. Apparent Magnitude: The apparent V-band magnitude through time of 282P. Observability: Our observability metric for Cerro Tololo Inter-American Observatory (CTIO), site code 807 (blue solid line) and the Lowell Discovery Telescope (LDT), site code G37 (orange dashed line), depicting the number of hours 282P was observable ($>15°$ above the horizon between sunset and sunrise) during a given universal time (UT) observing date. Opposition events and conjunctions result in maxima and minima concurrent with apparent magnitude, respectively. Temperature: Modeled temperature by date for the thermophysical extremes: a "flat slab" ($\chi = 1$, top line) and an isothermal body ($\chi = 4$, bottom line).

Results from the dynamical evolution of the 282P orbital clones are shown in Figures 3 and 4. For all plots, time $t = 0$ corresponds to Julian date (JD) 2459600.5 (UT 2022 Jan 21), and time ranges from $t = -250$ to $t = +350$ (1772–2372 AD). Horizontal lines at distances of one, three, and five Hill radii (Equation (1)) from Jupiter and Saturn are shown in Figure 4 panels (a) and (b). The Hill radius (Hill 1878) r_H is a metric of orbital stability and indicates the region where a secondary body (e.g., a planet) has dominant gravitational influence over a tertiary body (e.g., a moon), with both being related to a primary body, such as the Sun. At pericenter, the Hill radius of the secondary body can be approximated as

$$r_{\rm H} \approx a(1 - e)(m/3M)^{1/3}, \qquad (1)$$

where a, e, and m are the semimajor axis, eccentricity, and mass of the secondary (Jupiter or Saturn in our case), respectively, and M is the mass of the primary (here, the Sun). Close passages of a small body within a few Hill radii of a planet are generally considered to be significant perturbations

and may drastically alter the orbit of the small body (see Hamilton & Burns 1992 Section 2.1.2 for discussion).

From ∼180 yr ago until ∼300 yr in the future, the orbit of 282P is well-constrained in our simulations. Figure 4(a) illustrates that 282P has roughly 10 close encounters (within ∼2 au) with Jupiter, and one with Saturn, over the range $-250 < t < 350$ yr. These encounters have a strong effect on the semimajor axis a of 282P (Figure 3(b)), and, as illustrated by Figure 4(d), a noticeable influence on its Tisserand parameter with respect to Jupiter $T_{\rm J}$,

$$T_{\rm J} = \frac{a_{\rm J}}{a} + 2\cos(i)\sqrt{\frac{a}{a_{\rm J}}(1 - e^2)}, \qquad (2)$$

where $a_{\rm J}$ is the semimajor axis of Jupiter; and a, e, and i are the semimajor axis, eccentricity, and inclination of the body, respectively. $T_{\rm J}$ essentially describes an object's close approach speed to Jupiter or, in effect, the degree of dynamical perturbation an object will experience as a consequence of Jovian influence. $T_{\rm J}$ is often described as invariant (Kresák 1972) or conserved, meaning that changes in the orbital parameters still result in the same $T_{\rm J}$, although, in practice, its value does change slightly as a result of close encounters (see Figure 4(d)).

Due to the small Jupiter-centric distances of 282P during these encounters, compounded by its orbital uncertainties, the past orbit of 282P (prior to $t \approx -180$ yr) is chaotic. This dynamical chaos is plainly evident in all panels as orbital clones take a multitude of paths within the parameter space, resulting in a broad range of possible orbital outcomes due only to slight variations in initial 282P orbital parameters.

A consequential encounter with Saturn occurred around 1838 ($t \approx -184$ yr; Figure 4(b)), followed by another interaction with Jupiter in 1846 ($t = -176$ yr; Figure 4(a)). After these encounters 282P was a JFC (100% of orbital clones) with a semimajor axis between Jupiter's and Saturn's semimajor axes (Figure 3(b)), and crossing the orbits of both planets (Figure 4(c)). These highly perturbative passages placed 282P on the path that would lead to its current quasi-Hilda orbit.

In 1940 ($t = -82$ yr), 282P had a very close encounter with Jupiter, at a distance of 0.3 au—interior to one Hill radius. As seen in Figure 3(a), this encounter dramatically altered 282P's orbit, shifting 282P from an orbit primarily exterior to Jupiter to an orbit largely interior to Jupiter (Figure 3(b)). This same interaction also caused 282P's orbit to migrate from a Jupiter- and Saturn-crossing to only a Jupiter-crossing orbit (Figure 4(c)). This step in the orbital evolution of 282P also changed its $T_{\rm J}$ (Figure 4(d)) to be close to the traditional $T_{\rm J} = 3$ comet–asteroid dynamical boundary. At this point in time, 282P remained a JFC (100% of orbital clones) despite its dramatic change in orbit.

Around $t \approx 200$ yr, 282P crosses the $T_{\rm J} = 3$ boundary dividing the JFCs and the asteroids on the order of 10 times. Although no major changes in the orbit 282P occur during this time, because of the stringency of this boundary, relatively minor perturbations result in oscillation between dynamical classes.

After a major encounter with Jupiter around 2330 AD ($t \approx 308$ yrs), dynamical chaos again becomes dominant and remains so for the rest of the simulation. Following this encounter, the orbit of 282P does not converge around any single solution. Slight diffusion following the previous several
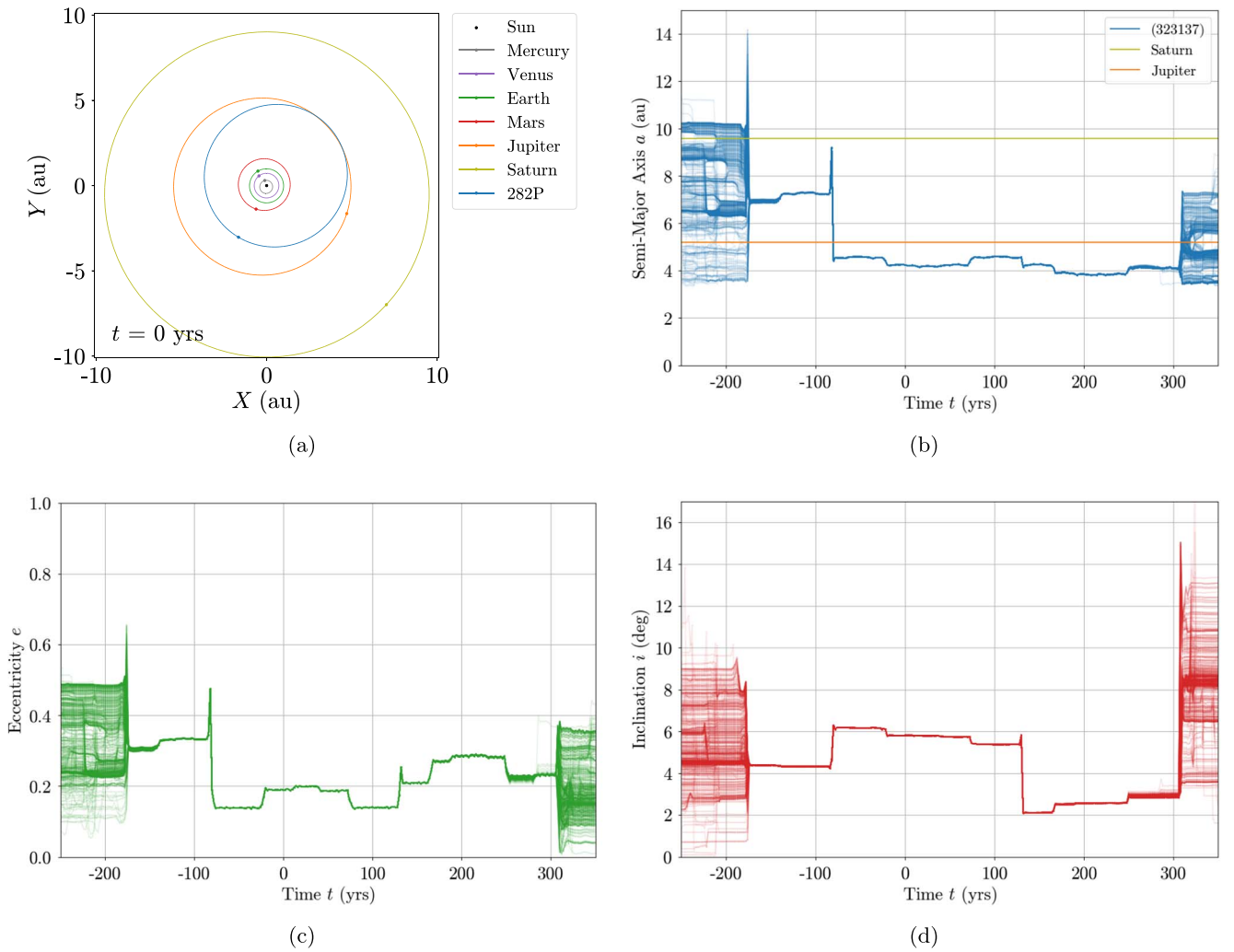
(a)

(b)

(c)

(d)

Figure 3. Results from dynamical integration of 282P orbital clones. For all plots, time $t = 0$ corresponds to UT 2022 January 21. Jovian and Saturnian close encounters prevent accurate orbital parameter determination outside $-180 \lesssim t \lesssim 300$ yrs, given known orbital uncertainties. (a) Orbital diagram for 282P and nearby planets; note that Uranus and Neptune were included in our simulations, but they are not shown here. (b) Semimajor axis a evolution. (c) Eccentricity e evolution. (d) Inclination i evolution.

Jupiter passages are also visible in Figures 3(b)–(d) and 4(a)–(d), and these also add uncertainty concerning encounters around 2301 to 2306 ($t \approx 280$ to 285 yr). Although we are unable to precisely determine past and future orbits of 282P outside of $-180 \lesssim t \lesssim 300$ because of dynamical chaos, we are able to examine the fraction of orbital clones that finish the simulation (forward and backward) on orbits associated with different orbital classes.

5. Dynamical Classifications: Past, Present, and Future

Minor planets are often classified dynamically, based on orbital characteristics such as semimajor axis. 282P was labeled a JFC by Hsieh et al. (2015), in agreement with a widely adopted system that classifies objects dynamically based on their Tisserand parameter with respect to Jupiter, T_J (Equation (2))

Via Equation (2), Jupiter's T_J is 2.998 given $a_J = 5.20$, $e_J = 0.049$, and $i_J = 0.013$. Notably, objects with $T_J > 3$ cannot cross the Jovian orbit; thus their orbits are entirely interior or exterior to Jupiter's orbit (Levison 1996). Objects with $T_J < 3$ are considered cometary (Levison 1996), while those with $T_J > 3$ are not (Vaghi 1973a, 1973b), a classification approach

first suggested by Carusi et al. (1987) and Levison (1996). JFCs have $2 < T_J < 3$ (see, e.g., Jewitt 2009), and Damocloids have $T_J < 2$ (Jewitt 2005). We note, however, that the traditional T_J asteroid—JFC—Damocloid continuum does not include (or exclude) QHOs.

As discussed in Section 1, we adopt the Jewitt (2009) definition of Centaur, which stipulates that a Centaur has an orbit entirely exterior to Jupiter, with both q and a interior to Neptune, and the body is not in 1:1 resonance with a planet. 282P has a semimajor axis $a = 4.240$ au, well interior to Jupiter's $a_J = 5.2$ au. This disqualifies 282P as presently on a Centaurian orbit.

Active objects other than comets orbiting interior to Jupiter are primarily active asteroids, defined as (1) $T_J > 3$, (2) displaying comet-like activity, and (3) orbiting outside of mean-motion resonance with any of the planets. This last stipulation rules out the Jupiter Trojans (1:1 resonance) and the Hildas (3:2 resonance with Jupiter), even though both classes have members above and below the $T_J = 3.0$ asteroid–comet transition line. We compute $T_J = 2.99136891 \pm (3.73 \times 10^{-8})$ for 282P (see Appendix C for a list of orbital parameters). These values do not exceed the traditional $T_J = 3$ cutoff; thus

5
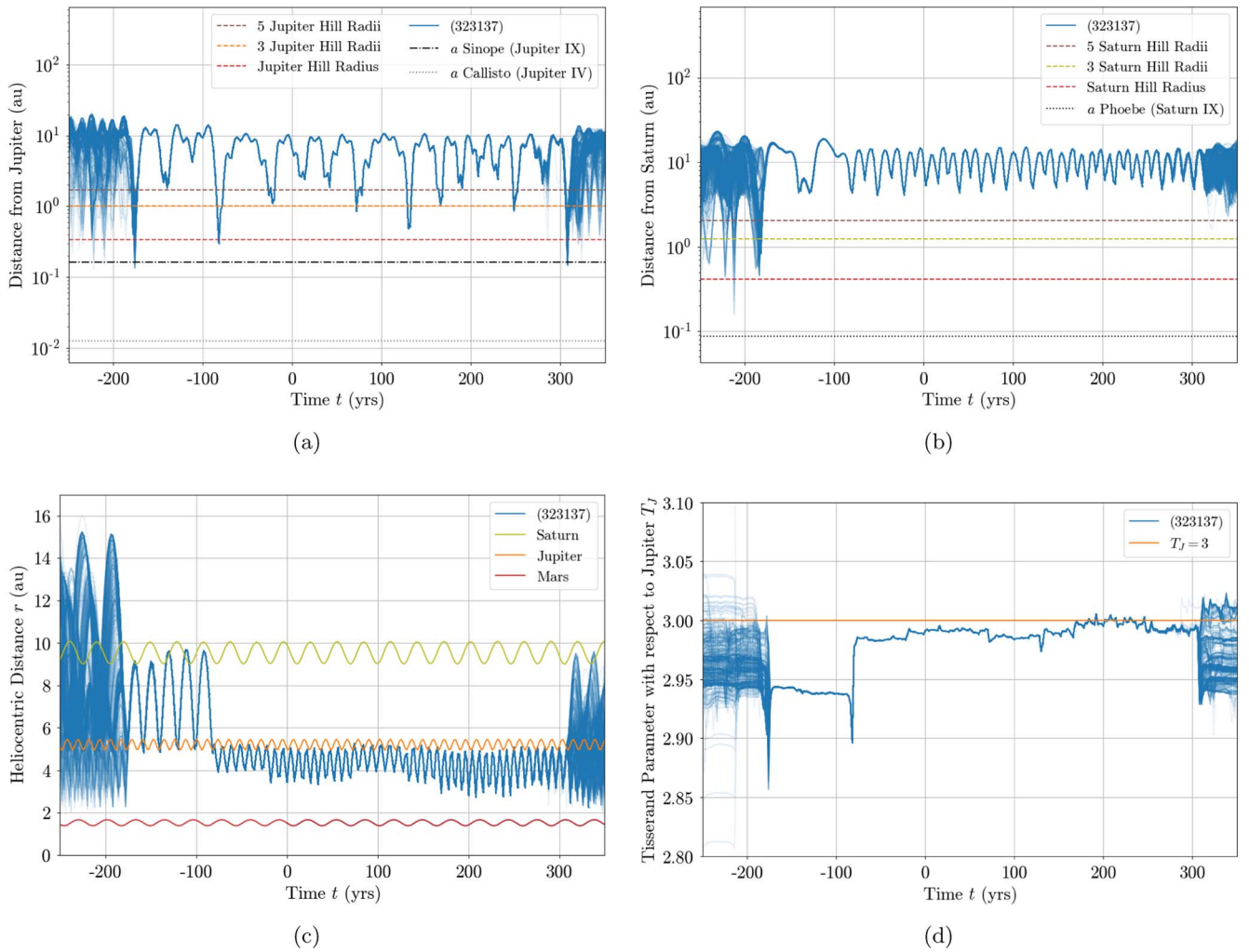
Figure 4. Additional results from dynamical integration of 282P orbital clones. For each plot, time $t = 0$ is UT 2022 January 21. Close encounters with Jupiter and Saturn are so significant that orbital elements cannot be accurately determined before/after $-180 \lesssim t \lesssim 300$ yr, given orbital uncertainties. (a) Distance between Jupiter and 282P as a function of time. Indicated Hill radii provide references for the degree of orbit alteration imparted by a close encounter. For reference, the semimajor axes of two Jovian moons are shown: Callisto, the outermost Galilean satellite, and Sinope (Nicholson 1914), a likely captured (Grav et al. 2003) distant irregular and retrograde Jovian moon. (b) Distance between Saturn and 282P as a function of time. The semimajor axis of the irregular Saturnian moon Phoebe, believed to be captured through close encounter (Johnson & Lunine 2005; Jewitt & Haghighipour 2007), is given for reference. (c) Heliocentric distance r evolution. (d) Tisserand parameter with respect to Jupiter T_J (Equation (2)), where the horizontal orange line representing $T_J = 3$ indicates the widely adopted boundary between comet-like and asteroid-like orbits.

282P cannot be considered an active asteroid in its current orbit. MBCs are an active asteroid subset defined as orbiting entirely within the main asteroid belt (Hsieh et al. 2015). Figure 4(c) shows that 282P's heliocentric distance does not stay within the boundaries of the Asteroid Belt (i.e., between the orbits of Mars and Jupiter), and so 282P does not qualify as an MBC.

Blurring the lines between JFC and Hilda is the quasi-Hilda regime. A quasi-Hilda, also referred to as a QHO, quasi-Hilda asteroid (QHA; Jewitt & Kim 2020), or quasi-Hilda comet (QHC), is a minor planet on an orbit similar to a Hilda (Toth 2006; Gil-Hutton & Garcia-Migani 2016). Hildas are defined by their 3:2 interior mean-motion resonance with Jupiter; however, quasi-Hildas are not in this resonance, though they do orbit near it. Quasi-Hildas likely migrated from the JFC region (see discussion in Jewitt & Kim 2020). We favor the term QHO or QHA over QHC, given that fewer than 15 quasi-Hildas have been found to be active, while the remainder of the >270 identified quasi-Hildas (Gil-Hutton & Garcia-Migani 2016) have

not been confirmed to be active. Notable objects from the quasi-Hilda class are 39P/Oterma (Oterma 1942), an object that was a quasi-Hilda prior to 1963, when a very close (0.095 au) encounter with Jupiter redirected the object into a Centuarian orbit. Another notable quasi-Hilda was D/Shoemaker-Levy 9, which famously broke apart and impacted Jupiter in 1994 (e.g., Weaver et al. 1995).

Quasi-Hildas have orbital parameters similar to that of the Hildas, approximately $3.7 \lesssim a \lesssim 4.2$ au, $e \leqslant 0.3$, and $i \leqslant 20°$. In rough agreement, 282P has $a = 4.24$ au, $e = 0.188$, and $i = 5°.8$ (Appendix C). Hildas are also known for their trilobal orbits as viewed in the Jupiter corotating frame (caused by their residence in the 3:2 interior mean-motion resonance with Jupiter), especially the namesake asteroid (153) Hilda (Figure 5(d)). Because (153) Hilda is in a stable 3:2 resonant orbit with Jupiter, its orbit remains roughly constant, with a small amount of libration over time. By contrast, quasi-Hildas like 246P/NEAT (Figure 5(e)) are near the same resonance and show signs of this characteristic trilobal pattern; however, their
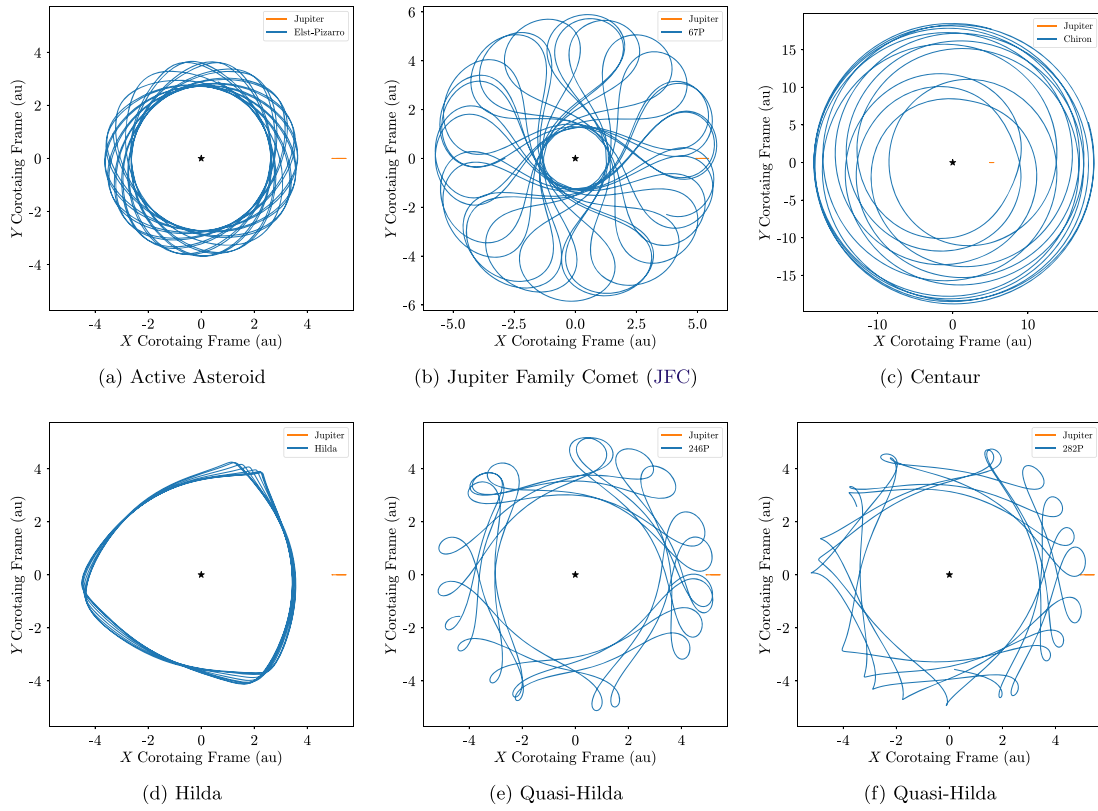
Figure 5. Orbital motion of minor planets (blue lines) as seen in the reference frame corotating with Jupiter (orange lines at right edge of plots). (a) MBC (7968) Elst-Pizarro (133P). (b) JFC 67P/Churyumov–Gerasimenko (previously visited by the European Space Agency (ESA) Rosetta Spacecraft). (c) Centaur (2060) Chiron (95P). (d) (153) Hilda, the namesake of the Hilda dynamical class, in the 3:2 interior mean-motion resonance with Jupiter. (e) Quasi-Hilda 246P/NEAT, also designated 2010 V$_2$ and 2004 F$_3$. (f) Our object of study, 282P, in its quasi-Hilda orbit.

orbits drift considerably on timescales of hundreds of years. 282P (Figure 5(f)) also displays a typical quasi-Hilda orbit as viewed in the Jupiter corotating reference frame.

In the past, prior to 250 yr ago, 52% (260) of the 500 orbital clones were JFCs, 48% (239) were Centaurs, 5% (26) were already QHOs, and one (0.2%) was an outer main-belt asteroid (OMBA). The most probable scenario prior to 250 yr ago was that it was either a JFC or a Centaur, two classes that trace their origins to the Kuiper Belt (see reviews, Morbidelli & Nesvorný 2020 and Jewitt 2009, respectively).

In the future, after 350 yr time, 81% (403) of clones become JFCs, 18% (90) remain QHOs, 14% (69) become OMBAs, and 5.6% (28) return to Centaurian orbits. Clearly the most likely scenario is that 282P will become a JFC; however, there are still significant possibilities that 282P remains a QHO or becomes an active OMBA.

6. Thermodynamical Modeling

In order to understand the approximate temperature ranges that 282P experiences over the course of its present orbit in order to (1) understand what role, if any, thermal fracture may play in the activity we observe, and (2) evaluate the likelihood of ices surviving on the surface, albeit with limited effect because of the narrow window (∼500 yr) of dynamically well-determined orbital parameters available (Section 4).

Following the procedure of Chandler et al. (2021; originally adapted from Hsieh et al. 2015), we compute the surface equilibrium temperature T_{eq} for 282P as a gray airless body. To accomplish this we begin with the water ice sublimation energy

balance equation

$$\frac{F_\odot}{r_h^2}(1 - A) = \chi[\varepsilon\sigma T_{eq}^4 + Lf_D\dot{m}_w(T_{eq})] \qquad (3)$$

with the solar constant $F_\odot = 1360$ W m^{-2}, heliocentric distance of the airless body r_h (au), and the body's assumed Bond albedo is $A = 0.05$; note that the true albedo could differ significantly from this value, and thus it would be helpful to measure the albedo in the future when 282P is inactive. The heat distribution over the body is accounted for by χ, which is bound by the coldest temperatures via the fast-rotating isothermal approximation ($\chi = 1$), and the hottest temperatures via the "slab" subsolar approximation, where one side of the object always faces the Sun. The assumed effective infrared emissivity is $\varepsilon = 0.9$, σ is the Stefan–Boltzmann constant, the latent heat of sublimation of water ice (which we approximate here as being independent of temperature) is $L = 2.83$ MJ kg^{-1}, the mantling-induced sublimation efficiency dampening is assumed to be $f_D = 1$ (absence of mantle), and the sublimation-driven water ice mass-loss rate in a vacuum $\dot{m}_w$ is given by

$$\dot{m}_w = P_v(T)\sqrt{\frac{\mu}{2\pi kT}} \qquad (4)$$

where the mass of one water molecule is $\mu = 2.991 \cdot 10^{-26}$ kg, k is the Boltzmann constant, and the vapor pressure (in Pa) as a function of temperature $P_v(T)$ is derived from the

Clausius–Clapeyron relation,

$$P_v(T) = 611 \times \exp\left[\frac{\Delta H_{subl}}{R_g}\left(\frac{1}{273.16} - \frac{1}{T} \right) \right] \quad (5)$$

where the heat of sublimation of ice to vapor is $\Delta H_{subl} = 51.06$ MJ kmol^{-1}, and the ideal gas constant is $R_g = 8.314 \times 10^{-3}$ MJ kmol^{-1} K^{-1}.

Solving Equations (3)—(5) for the body's heliocentric distance r_h (in au) as a function of the equilibrium temperature T_{eq} and χ yields

$$r_h(T_{eq}, \chi) = \frac{F_\odot(1 - A)\chi^{-1}}{\epsilon\sigma T_{eq}^4 + Lf_D \cdot 611 \; e^{\frac{\Delta H_{subl}}{R_G}\left(\frac{1}{273.16K} - \frac{1}{T_{eq}}\right)}} \quad (6)$$

We translate Equation (6) to a function of the equilibrium temperature T_{eq} by computing r_h for an array of values (100 K to 300 K in this case), then fit a model to these data with a SciPy (Virtanen et al. 2020; Python package) univariate spline. Using this model we compute 282P temperatures for 282P heliocentric distances from perihelion and aphelion. with this function to arrive at temperatures for 282P over the course of its orbit.

Figure 2 (bottom panel) shows the temperature evolution for the maximum and minimum solar heating distribution scenarios ($\chi = 1$ and $\chi = 4$, respectively) for 282P from 2012 through 2024. Temperatures range between roughly 175 K and 220 K for $\chi = 1$, or 130 K and 160 K for $\chi = 4$, with a ~45 K maximum temperature variation in any one orbit. 282P spends some ($\chi = 4$) or all ($\chi = 1$) of its time with surface temperatures above 145 K. Water ice is not expected to survive above this temperature on Gyr timescales (Schorghofer 2008; Snodgrass et al. 2017); however, we showed in Section 4 that, prior to ~80 yr ago, 282P had a semimajor axis of $a > 6$ au, a region much colder than 145 K. Even if 282P had spent most of its life with temperatures at the high end of our computed temperatures (>220 K), water ice can survive on Gyr timescales at shallow (a few centimeter) depths (Schorghofer 2008; Prialnik & Rosenberg 2009). Some bodies, such as (24) Themis, have been found to have surface ices (Campins et al. 2010; Rivkin & Emery 2010), which suggests that an unknown mechanism may replenish surface ice with subsurface volatiles. In this case the ice lifetimes could be greatly extended.

7. Activity Mechanism

Infrequent stochastic events, such as impacts (e.g., (596) Scheila; Bodewits et al. 2011; Ishiguro et al. 2011; Moreno et al. 2011), are highly unlikely to be the activity mechanism given the multiepoch nature of the activity we identified in this work. Moreover, it is unlikely that activity ceased during the 15 month interval between the UT 2021 March 14 archival activity and our UT 7 June 2022 Gemini South activity observations (Section 3), when 282P was at a heliocentric distance $r_H = 3.548$ au and $r_H = 3.556$ au, respectively, and 282P was only closer to the Sun in the interim. Similarly, our archival data show that activity lasted ~15 months during the 2012–2013 apparition.

Recurrent activity is most commonly caused by volatile sublimation (e.g., 133P; Boehnhardt et al. 1996; Hsieh et al. 2004) or rotational instability (e.g., (6478) Gault; Kleyna et al. 2019; Chandler et al. 2019). Rotational instability is impossible

to rule out entirely for 282P because its rotation period is unknown. However, (1) no activity attributed to rotational stability for any object has been observed to be continuous for as long as the 15 month episodes we report, and (2) rotational instability is not correlated with perihelion passage. It is worth noting that there are not yet many known objects with activity attributed to rotational disruption, so it is still difficult to draw firm conclusions about the behavior of those objects. In any case it would be useful to measure a rotation period for 282P to help assess potential influence of rotational instability in the observed activity of 282P. The taxonomic class of 282P is unknown, but should 282P be classified as a member of a desiccated spectral class (e.g., S type), then sublimation would not likely be the underlying activity mechanism. Color measurements or spectroscopy when 282P is quiescent would help determine its spectral class.

A caveat, however, is that many of our archival images were taken when 282P was significantly fainter than the images showing activity (Figure 2), thereby making activity detection more difficult than if 282P was brighter. Consequently, archival images showing 282P were predominantly taken near its perihelion passage. The farthest evidently quiescent image of 282P was taken when it was at ~4 au (Figure 2). Thus we cannot state with total certainty that 282P was inactive elsewhere in its orbit.

Thermal fracture can cause repeated activity outbursts. For example, (3200) Phaethon undergoes 600 K temperature swings, peaking at 800 K–1100 K, exceeding the serpentine-phyllosilicate decomposition threshold of 574 K (Ohtsuka et al. 2009) and potentially causing thermal fracture (Licandro et al. 2007; Kasuga & Jewitt 2008) including mass loss (Li & Jewitt 2013; Hui & Li 2017). Temperatures on 282P reach at most ~220 K (Figure 2), with ~45 K being the maximum variation. Considering the relatively low temperatures and mild temperature changes we (1) consider it unlikely that 282P activity is due to thermal fracture, and (2) reaffirm that thermal fracture is generally considered a nonviable mechanism for any objects other than NEOs.

Overall, we find volatile sublimation on 282P the most likely activity mechanism, because (1) it is unlikely that an object originating from the Kuiper Belt such as 282P would be desiccated, (2) archival and new activity observations are from when 282P was near perihelion (Figure 2), a characteristic diagnostic of sublimation-driven activity (e.g., Hsieh et al. 2012), and (3) 15 months of continuous activity has not been reported for any other activity mechanism (e.g., rotational instability, impact events) to date, let alone two such epochs.

8. Summary and Future Work

This study was prompted by Citizen Scientists from the NASA Partner program *Active Asteroids* classifying two images of 282P from 2021 March as showing activity. Two additional images by astronomers Roland Fichtl and Michael Jäger brought the total number of images (from UT 2021 March 31 and UT 2021 April 4) to four. We conducted follow-up observations with the Gemini South 8.1 m telescope on UT 2022 June 7 and found 282P still active, indicating it has been active for >15 months during the current 2021–2022 activity epoch. Our archival investigation revealed the only other known apparition, from 2012 to 2013, also spanned ~15 months. Together, our new and archival data demonstrate 282P

has been active during two consecutive perihelion passages, consistent with sublimation-driven activity.

We conducted extensive dynamical modeling and found 282P has experienced a series of ∼5 strong interactions with Jupiter and Saturn in the past, and that 282P will again have close encounters with Jupiter in the near future. These interactions are so strong that dynamical chaos dominates our simulations prior to 180 years ago and beyond 350 years in the future, but we are still able to statistically quantify a probable orbital class for 282P prior to −180 yr (52% JFCs, 48% Centaur) and after +350 yr (81% JFCs, 18% QHO, 14% OMBA). We classify present-day 282P as a quasi-Hilda Object (QHO).

We carried out thermodynamical modeling that showed that 282P undergoes temperatures ranging at most between 135 K and 220 K, too mild for thermal fracture but warm enough that surface water ice would not normally survive on timescales of the solar system lifetime. However, 282P arrived at its present orbit recently; prior to 1941, 282P was primarily exterior to Jupiter's orbit and, consequently, sufficiently cold for water ice to survive on its surface. Given that both activity apparitions (Epoch I: 2012–2013 and Epoch II: 2021–2022) each lasted over 15 months, and both outbursts spanned perihelia passage, we determine the activity mechanism to most likely be volatile sublimation.

Coma likely accounts for the majority of the reflected light we observe emanating from 282P, so it is infeasible to determine the color of the nucleus and, consequently, 282P's spectral class (e.g., C type, S type). Measuring its rotational period would also help assess what (if any) role rotational instability plays in the observed activity. Specifically, a rotation period faster than the spin-barrier limit of two hours would indicate breakup.

Most images of 282P were taken when it was near perihelion passage (3.441 au), though there were observations from Epoch I that showed 282P clearly, without activity, when it was beyond ∼4 au. 282P is currently outbound and will again be beyond 4 au in mid-2023 and, thus, likely inactive; determining if/when 282P returns to a quiescent state would help bolster the case for sublimation-driven activity because activity occurring preferentially near perihelion, and a lack of activity elsewhere, is characteristic of sublimation-driven activity.

282P is currently observable, especially from the southern hemisphere; however, the object is passing in front of dense regions of the Milky Way until the end of 2022 November (see Lowell `AstFinder`[4] finding charts). 282P will be in a less dense region of the Milky Way and be observable, in a similar fashion to our Gemini South observations (Section 3) on UT 2022 September 26 for ∼12 days, carefully timed for sky regions with fewer stars. As Earth's orbit progresses around the Sun, 282P becomes observable for less time each night through 2022 November, until UT 2022 December 26, when it becomes observable only during twilight. Observations during this window would help constrain the timeframe for periods of quiescence.

Facilities: Astro Data Archive, Blanco (DECam), CFHT (MegaCam), Gaia, Gemini-South (GMOS-S), IRSA, LDT (LMI), Magellan: Baade (TSIP), PO:1.2 m (PTF, ZTF), PS1, Sloan, VATT (VATT4K), VST (OmegaCAM).

Software: astropy (Robitaille et al. 2013), astrometry.net (Lang et al. 2010), FTOOLS[5], IAS15 integrator (Rein & Spiegel 2015), JPL Horizons (Giorgini et al. 1996), Matplotlib (Hunter 2007), NumPy (Harris et al. 2020), pandas (McKinney 2010; Reback et al. 2022), REBOUND (Rein & Liu 2012; Rein et al. 2019), SAOImageDS9 (Joye 2006), SciPy (Virtanen et al. 2020), Siril[6], SkyBot (Berthier et al. 2006), termcolor[7], tqdm (da Costa-Luis et al. 2022), Vizier (Ochsenbein et al. 2000).

Appendix A

In Table A1 we list details of the observations included in this work. Associated data sources are given in Appendix B.

Table A1
Table of Observations

Figure[a]	Act.[b]	Obs. Date[c]	Source	N[d]	Exp. [s][e]	Filter(s)	V[f]	r [au][g]	STO [°][h]	ν [°][i]	%$_{Q \to q}$[j]	Note[k]
		04 Feb 2011	PS1	2	40	r	19.7	4.26	3.3	258.1	84%	1
		16 Feb 2012	PS1	1	45	i	19.3	3.69	8.9	306.4	95%	1
		24 Feb 2012	PS1	1, 1	43, 40	g, r	19.2	3.68	6.9	307.6	95%	1
		26 Feb 2012	PS1	2	40	r	19.2	3.67	6.3	307.9	96%	1
1e	Y	28 Mar 2012	MegaPrime	2	120	r	18.9	3.64	3.2	312.6	96%	2
	Y	05 Jul 2012	OmegaCAM	4	240	i	20.1	3.54	16.1	328.0	98%	3
		14 Apr 2013	PS1	2	45	i	19.3	3.47	12.8	14.9	99%	1
		22 Apr 2013	PS1	2	30	z	19.2	3.47	11.1	16.3	99%	1
1f	Y	05 May 2013	DECam	2	150	r	19.5	3.48	12.9	318.4	97%	4
	Y	15 May 2013	PS1	1	43	g	18.8	3.48	5.2	20.1	99%	1
1g	Y	13 Jun 2013	MegaPrime	10	120	r	18.8	3.50	4.9	24.8	99%	5
		03 Aug 2013	PS1	2	80, 60	y, z	19.6	3.54	15.3	33.0	98%	1
		11 Jun 2014	PS1	2	45	i	20.0	3.95	12.5	78.1	90%	1
		14 Aug 2014	PS1	3	45	i	19.4	4.05	3.3	86.1	88%	1
		15 Aug 2014	PS1	4	45	i	19.4	4.04	3.5	86.2	88%	1
		04 Jan 2021	ZTF	1	30	r	20.0	3.63	15.7	312.5	96%	6
		07 Jan 2021	ZTF	1	30	g	20.0	3.63	15.7	312.9	96%	6
		09 Jan 2021	ZTF	1	30	r	20.0	3.62	15.7	313.2	96%	6
1(a)	Y	14 Mar 2021	DECam	1	90	i	18.9	3.55	6.1	323.1	98%	7
1h	Y	17 Mar 2021	DECam	1	90	i	18.9	3.55	5.2	323.6	98%	7
1(b)	Y	31 Mar 2021	QHY600	1	2160	UV/IR	18.5	3.54	0.7	325.9	98%	8
1(c)	Y	04 Apr 2021	CDS-5D	1	1500	(none)	18.5	3.54	0.5	326.4	98%	9
		07 Mar 2022	IMACS	5	10	WB4800-7800	20.0	3.48	16.3	22.3	99%	10
		21 May 2022	LDT	3	90	VR, i	19.1	3.54	8.3	34.4	98%	11
1(d)	Y	07 Jun 2022	GMOS-S	6, 6, 6	120	g,r,i	18.8	3.56	3.8	37.2	98%	12

Notes.
[a] Figure showing the image.
[b] Activity identified in image(s).
[c] UT date of observation.
[d] Number of images.
[e] Exposure time.
[f] Apparent V-band magnitude (Horizons).
[g] Heliocentric distance.
[h] Sun–target–observer angle.
[i] True anomaly.
[j] Percentage to perihelion q from aphelion Q, defined by $\%_{T \to q} = \left(\dfrac{Q - r}{Q - q} \right) \cdot 100\%$.
[k] Note number.

1: PS1 is the Panoramic Survey Telescope and Rapid Response System (Pan-STARRS) One. 2: Prop. ID 12AH16, PI Wainscoat. 3: Prop. ID 177.A-3016(D), PI Kuijken. 4: Dark Energy Camera (DECam); Prop. ID 2013A-0327, PI Rest. 5: Prop. ID 13AH09, PI Wainscoat. 6: Zwicky Transient Facility (ZTF); Prop. ID 1467501130115, PI Kulkarni; data acquired through ZTF Alert Stream service (Patterson et al. 2019). 7: Prop. ID 2019A-0305, PI Drlica-Wagner. 8: Michael Jäger (Weißenkirchen, Austria), QHY600 charge-coupled device (CCD) on a 14″ Newtonian. 9.: Roland Fichtl (Engelhardsberg, Germany), Central DS brand modified cooled Canon 5D Mark III on a 0.4 m f/2.5 Newtonian; http://www.dieholzhaeusler.de/Astro/comets/0282P.htm. 10: Inamori-Magellan Areal Camera and Spectrograph (IMACS); PI Trujillo. 11: Inamori-Magellan Areal Camera and Spectrograph (IMACS); PI Trujillo. 12: Gemini Multi-Object Spectrograph (GMOS); Prop. ID GS-2022A-DD-103, PI Chandler.

---

[5] https://heasarc.gsfc.nasa.gov/ftools/

[6] https://siril.org
[7] https://pypi.org/project/termcolor

Appendix B

Table B1 lists the instruments and telescopes used in this work, along with their respective pixel scales, locations, and data archives.

Table B1
Equipment and Archives

Instrument	Telescope	Pixel Scale [″/pix]	Location	AstroArchive	ESO	SSOIS	STScI	IRSA
DECam	4.0 m Blanco	0.263	Cerro Tololo, Chile	S,R		S		
GMOS-S	8.1 m Gemini South	0.080	Cerro Pachón, Chile					
IMACS	6.5 m Baade	0.110	Las Campanas, Chile					
OmegaCAM	2.6 m VLT Survey	0.214	Cerro Paranal, Chile		R	S		
GigaPixel1	1.8 m Pan-STARRS1	0.258	Haleakalā, Hawaii			S	R	
LMI	4.3 m LDT	0.120	Happy Jack, Arizona					
MegaPrime	3.6 m CFHT	0.185	Maunakea, Hawaii			S,R		
PTF/CFHT12K	48″ Samuel Oschin	1.010	Mt. Palomar, California					S,R
ZTF Camera	48″ Samuel Oschin	1.012	Mt. Palomar, California					S,R
VATT4K CCD	1.8 m VATT	0.188	Mt. Graham, Arizona					

Note. R indicates the repository for data retrieval. S indicates the search capability. AstroArchive: NSF National Optical and Infrared Laboratory (NOIRLab) AstroArchive (https://astroarchive.noirlab.edu). European Space Organization (ESO): European Space Organization (https://archive.eso.org). IRSA: NASA/CalTech IRSA (https://irsa.ipac.caltech.edu). PTF: The Palomar Transient Factory (PTF). SSOIS: The Solar System Object Information Search (SSOIS; Gwyn et al. 2012, https://www.cadc-ccda.hia-iha.nrc-cnrc.gc.ca/en/ssois/). Space Telescope Science Institute (STScI): https://www.stsci.edu/.

Appendix C
282P/(323137) 2003 BM80 Data

We provide information current as of 2022 March 18 regarding 282P/(323137) 2003 BM$_{80}$ in Table C1.

Table C1
282P Properties

Parameter	Value	Source
Designations	(323137), 2003 BM$_{80}$, 2003 FV$_{112}$, 282P	JPL SBDB, MPC
Discovery Date	2003 January 31	JPL SBDB, MPC
Discovery Observer(s)	LONEOS	JPL SBDB, MPC
Discovery Observatory	Lowell Observatory	JPL SBDB, MPC
Discovery Site	Anderson Mesa Station, Arizona	JPL SBDB, MPC
Discovery Site Code	688	MPC
Activity Discovery Date	2013 June 12	CBET 3559 (Bolin et al. 2013)
Activity Discoverer(s)	Bryce Bolin, Larry Denneau, Peter Veres	CBET 3559 (Bolin et al. 2013)
Orbit Type	Quasi-Hilda Object (QHO)	this work
Diameter	$D = 3.4 \pm 0.4$ km	Harris & Lagerros (2002)
Absolute V-band Magnitude	$H = 13.63$	MPC (MPO648742)
Geometric Albedo	Unknown	
Assumed Geometric Albedo	4%	Snodgrass et al. (2011)
Rotation Period	Unknown	
Orbital Period	$P = 8.732 \pm (2.174 \times 10^{-7})$ yr	JPL SBDB
Semimajor Axis	$a = 4.240 \pm (7.039 \times 10^{-8})$ au	JPL SBDB
Perihelion Distance	$q = 3.441 \pm (3.468 \times 10^{-7})$ au	JPL SBDB
Aphelion Distance	$Q = 5.039 \pm (8.366 \times 10^{-8})$ au	JPL SBDB
Eccentricity	$e = 0.188 \pm (7.790 \times 10^{-8})$	JPL SBDB
Inclination	$i = 5.812° \pm (1.166° \times 10^{-5})$	JPL SBDB
Argument of Perihelion	$\omega = 217.626° \pm (7.816° \times 10^{-5})$	JPL SBDB
Longitude of Ascending Node	$\Omega = 9.297° \pm (5.974° \times 10^{-5})$	JPL SBDB
Mean Anomaly	$M = 9.979° \pm (3.815° \times 10^{-5})$	JPL SBDB
Tisserand Parameter w.r.t. Jupiter	$T_J = 2.99136891 \pm (3.73 \times 10^{-8})$	this work
Orbital Solution Date	2021 October 8	JPL SBDB

Note. Central Bureau for Electronic Telegrams (CBET; http://www.cbat.eps.harvard.edu). Jet Propulsion Laboratory (JPL) Small Body Database (SBDB) is the NASA JPL Small Body Database (https://ssd.jpl.nasa.gov/tools/sbdb_lookup.html. MPC is the Minor Planet Center (https://minorplanetcenter.net).

ORCID iDs

Colin Orion Chandler ● https://orcid.org/0000-0001-7335-1715
William J. Oldroyd ● https://orcid.org/0000-0001-5750-4953
Chadwick A. Trujillo ● https://orcid.org/0000-0001-9859-0894

References

Agarwal, J., Jewitt, D., Mutchler, M., Weaver, H., & Larson, S. 2017, Natur, 549, 357
Ahn, C. P., Alexandroff, R., Allende Prieto, C., et al. 2012, ApJS, 203, 21
Arnaboldi, M., Capaccioli, M., Mancini, D., et al. 1998, Msngr, 93, 30
Berthier, J., Vachier, F., Thuillot, W., et al. 2006, in ASP Conf. Ser. 351, Astronomical Data Analysis Software and Systems XV, ed. C. Gabriel et al. (San Francisco, CA: ASP), 367
Bodewits, D., Kelley, M. S., Li, J. Y., et al. 2011, ApJL, 733, L3
Boehnhardt, H., Schulz, R., Tozzi, G. P., Rauer, H., & Sekanina, Z. 1996, IAUC, 6495, 2
Bolin, B., Denneau, L., Veres, P., et al. 2013, CBET, 3559, 1
Bowell, E., Muinonen, K., & Wasserman, L. H. 1994, in IAU Symp. 160, Asteroids, comets, meteors, ed. A. Milani, M. Di Martino, & A. Cellino (Dordrecht: Kluwer), 477
Campins, H., Hargrove, K., Pinilla-Alonso, N., et al. 2010, Natur, 464, 1320
Carusi, A., Kresak, L., Perozzi, E., & Valsecchi, G. B. 1987, A&A, 187, 899
Chandler, C. O. 2022, PhD Thesis, Northern Arizona Univ., arXiv:2208.12364
Chandler, C. O., Curtis, A. M., Mommert, M., Sheppard, S. S., & Trujillo, C. A. 2018, PASP, 130, 114502
Chandler, C. O., Kueny, J., Gustafsson, A., et al. 2019, ApJL, 877, L12
Chandler, C. O., Kueny, J. K., Trujillo, C. A., Trilling, D. E., & Oldroyd, W. J. 2020, ApJL, 892, L38
Chandler, C. O., Trujillo, C. A., & Hsieh, H. H. 2021, ApJL, 922, L8
Collaboration, G., Brown, A. G. A., Vallenari, A., et al. 2018, A&A, 616, A1
Cunningham, L. E. 1950, IAUC, 1250, 3
da Costa-Luis, C., Larroque, S. K., Altendorf, K., et al. 2022, Tqdm: A Fast, Extensible Progress Bar for Python and CLI, Zenodo, doi:10.5281/zenodo.6412640
de Jong, J. T. A., Verdoes Kleijn, G. A., Boxhoorn, D. R., et al. 2015, A&A, 582, A62
Dressler, A., Bigelow, B., Hare, T., et al. 2011, PASP, 123, 288
Gil-Hutton, R., & Garcia-Migani, E. 2016, A&A, 590, A111
Gimeno, G., Roth, K., Chiboucas, K., et al. 2016, Proc. SPIE, 9908, 99082S
Giorgini, J. D., Yeomans, D. K., Chamberlin, A. B., et al. 1996, AAS, 28, 25.04
Grav, T., Holman, M. J., Gladman, B. J., & Aksnes, K. 2003, Icar, 166, 33
Gwyn, S. D. J., Hill, N., & Kavelaars, J. J. 2012, PASP, 124, 579
Hamilton, D. P., & Burns, J. A. 1992, Icar, 96, 43
Harris, A. W., & Lagerros, J. S. V. 2002, in Asteroids III, ed. W. F. Bottke et al. (Tucson, AZ: Univ. Arizona Press), 205
Harris, C. R., Millman, K. J., van der Walt, S. J., et al. 2020, Natur, 585, 357
Hill, G. W. 1878, AmJM, 1, 5
Hook, I. M., Jørgensen, I., Allington-Smith, J. R., et al. 2004, PASP, 116, 425
Hsieh, H. H., Denneau, L., Wainscoat, R. J., et al. 2015, Icar, 248, 289
Hsieh, H. H., Ishiguro, M., Kim, Y., et al. 2018, AJ, 156, 223
Hsieh, H. H., & Jewitt, D. 2006, Sci, 312, 561
Hsieh, H. H., Jewitt, D. C., & Fernández, Y. R. 2004, AJ, 127, 2997
Hsieh, H. H., Yang, B., & Haghighipour, N. 2012, ApJ, 744, 9
Hui, M. T., & Li, J. 2017, AJ, 153, 23
Hunter, J. D. 2007, CSE, 9, 90
Ishiguro, M., Hanayama, H., Hasegawa, S., et al. 2011, ApJL, 740, L11
Jewitt, D. 2005, AJ, 129, 530
Jewitt, D. 2009, AJ, 137, 4296
Jewitt, D., & Haghighipour, N. 2007, ARA&A, 45, 261
Jewitt, D., Hsieh, H., & Agarwal, J. 2015, in Asteroids IV, ed. P. Michel, F. E. DeMeo, & W. F. Bottke (Tucson, AZ: Univ. Arizona Press), 221
Jewitt, D., & Hsieh, H. H. 2022, arXiv:2203.01397
Jewitt, D., & Kim, Y. 2020, PSJ, 1, 77
Johnson, T. V., & Lunine, J. I. 2005, Natur, 435, 69
Joye, W. A. 2006, in ASP Conf. Ser. 351, Astronomical Data Analysis Software and Systems XV, ed. C. Gabriel et al. (San Francisco, CA: ASP), 574
Kasuga, T., & Jewitt, D. 2008, AJ, 136, 881
Kleyna, J. T., Hainaut, O. R., Meech, K. J., et al. 2019, ApJL, 874, L20
Kowal, C. T., & Gehrels, T. 1977, IAUC, 3129, 1
Kresák, L. 1972, BAICz, 23, 1
Kuijken, K. 2011, Msngr, 146, 8
Kuijken, K., Bender, R., Cappellaro, E., et al. 2002, Msngr, 110, 15
Lang, D., Hogg, D. W., Mierle, K., Blanton, M., & Roweis, S. 2010, AJ, 139, 1782
Levison, H. F. 1996, in ASP Conf. Proc. 107, Completing the Inventory of the Solar System, ed. T. W. Rettig & J. M. Hahn (San Francisco, CA: ASP), 173
Li, J., & Jewitt, D. 2013, AJ, 145, 154
Licandro, J., Campins, H., Mothe-Diniz, T., Pinilla-Alonso, N., & de Leon, J. 2007, A&A, 461, 751
McKinney, W. 2010, in Python in Science Conference, Austin, Texas, ed. S. van der Walt & J. Millman, 56, https://conference.scipy.org/proceedings/scipy2010/pdfs/mckinney.pdf
Morbidelli, A., & Nesvorný, D. 2020, in Kuiper Belt: Formation and Evolution, ed. D. Prialnik, M. A. Barucci, & L Young (Amsterdam: Elsevier), 25
Moreno, F., Licandro, J., Ortiz, J. L., et al. 2011, ApJ, 738, 130
Moskovitz, N., Burt, B., Schottland, R., et al. 2021, BAAS, 53, 101.04
Nicholson, S. B. 1914, PASP, 26, 197
Ochsenbein, F., Bauer, P., & Marcout, J. 2000, A&AS, 143, 23
Ohtsuka, K., Nakato, A., Nakamura, T., et al. 2009, PASJ, 61, 1375
Oterma, L. 1942, IAUC, 4, 900
Patterson, M. T., Bellm, E. C., Rusholme, B., et al. 2019, PASP, 131, 018001
Prialnik, D., & Rosenberg, E. D. 2009, MNRAS: Letters, 399, L79
Reback, J., jbrockmendel, McKinney, W., et al. 2022, Pandas-Dev/Pandas: Pandas 1.4.2, Zenodo, doi:10.5281/zenodo.6408044
Rein, H., Hernandez, D. M., Tamayo, D., et al. 2019, MNRAS, 485, 5490
Rein, H., & Liu, S.-F. 2012, A&A, 537, A128
Rein, H., & Spiegel, D. S. 2015, MNRAS, 446, 1424
Rivkin, A. S., & Emery, J. P. 2010, Natur, 464, 1322
Robitaille, T. P., Tollerud, E. J., Greenfield, P., et al. 2013, A&A, 558, A33
Schorghofer, N. 2008, ApJ, 682, 697
Schwassmann, A., & Wachmann, A. A. 1927, Bureau Central Astronomique de l'Union Astronomique Internationale Observatoire de Copenhague, 127, 171
Snodgrass, C., Agarwal, J., Combi, M., et al. 2017, A&ARv, 25, 5
Snodgrass, C., Fitzsimmons, A., Lowry, S. C., & Weissman, P. 2011, MNRAS, 414, 458
Toth, I. 2006, A&A, 448, 1191
Vaghi, S. 1973a, A&A, 24, 41
Vaghi, S. 1973b, A&A, 29, 85
Virtanen, P., Gommers, R., Oliphant, T. E., et al. 2020, Nat. Methods, 17, 261
Weaver, H. A., A'Hearn, M. F., Arpigny, C., et al. 1995, Sci, 267, 1282